Molecule-Level g-C$_3$N$_4$ Coordinated Transition Metals as a New Class of Electrocatalysts for Oxygen Electrode Reactions

Yao Zheng,[†,‖] Yan Jiao,[†,‖] Yihan Zhu,[‡] Qiran Cai,[§] Anthony Vasileff,[†] Lu Hua Li,[§] Yu Han,[‡] Ying Chen,[§] and Shi-Zhang Qiao*,[†]

[†]School of Chemical Engineering, University of Adelaide, Adelaide, SA 5005, Australia

[‡]Advanced Membrane and Porous Materials Center, Physical Science and Engineering Division, King Abdullah University of Science and Technology, Thuwal 23955-6900, Saudi Arabia

[§]Institute for Frontier Materials, Deakin University, Waurn Ponds, VIC 3216, Australia

⑤ *Supporting Information*

ABSTRACT: Organometallic complexes with metal–nitrogen/carbon (M–N/C) coordination are the most important alternatives to precious metal catalysts for oxygen reduction and evolution reactions (ORR and OER) in energy conversion devices. Here, we designed and developed a range of molecule-level graphitic carbon nitride (g-C$_3$N$_4$) coordinated transition metals (M–C$_3$N$_4$) as a new generation of M–N/C catalysts for these oxygen electrode reactions. As a proof-of-concept example, we conducted theoretical evaluation and experimental validation on a cobalt–C$_3$N$_4$ catalyst with a desired molecular configuration, which possesses comparable electrocatalytic activity to that of precious metal benchmarks for the ORR and OER in alkaline media. The correlation of experimental and computational results confirms that this high activity originates from the precise M–N$_2$ coordination in the g-C$_3$N$_4$ matrix. Moreover, the reversible ORR/OER activity trend for a wide variety of M–C$_3$N$_4$ complexes has been constructed to provide guidance for the molecular design of this promising class of catalysts.

The electrocatalytic oxygen reduction reaction (ORR) and oxygen evolution reaction (OER) are the heart of electrochemical energy conversion processes. Due to their multistep proton-coupled electron transfer reaction pathways, these two oxygen electrode reactions exhibit naturally sluggish kinetics and are much more energy costly than their counter hydrogen electrode reactions in respective devices. Therefore, precious metal-based catalysts are typically selected to achieve favorable reaction rates for the ORR and OER.[1] As alternatives, many nonprecious metal compounds with specific molecular/atomic configurations possess comparable performances to these precious metals. For example, nanostructured Fe- and Co-based metal–nitrogen/carbon (M–N/C) complexes are one of the most representative catalysts for the ORR and OER respectively.[1a,2] The electrocatalytic activities of these M–N/C materials strongly depend on the type of metal–N$_2$/N$_4$ edge defects and the nature of the macrocyclic ligand, which always need advanced synthetic approaches and precisely controlled chemical composition.[1,2] From a fundamental perspective, due to the complexity of various nanostructures and metal

coordination compositions, knowledge of the nature of active sites in these M–N/C materials is lacking.[3]

Graphitic carbon nitride (g-C$_3$N$_4$), with a graphene like framework, contains periodic heptazine units connected via tertiary amines (Figure S1).[4] The high level of pyridine-like nitrogen in heptazine heterorings provide rich electron lone pairs to capture metal ions in the ligands.[5] Therefore, unlike M–N/C materials, which always contain complicated nitrogen species but in low concentration, g-C$_3$N$_4$ can provide abundant and more uniform nitrogen coordinators. This will not only provide more metal coordination sites but also, more importantly, provide more precise information for the identification of catalytically active sites. As a result, although g-C$_3$N$_4$ itself is inert for electrocatalysis, there are reports regarding the metal–g-C$_3$N$_4$ complex (M–C$_3$N$_4$) for electrocatalytic processes.[5,6] However, there are still several issues unsolved: (i) the fine structure of metal coordination in g-C$_3$N$_4$ ligand is completely unknown; as a result, the catalytic nature and activity origin of M–C$_3$N$_4$ catalysts remain elusive; (ii) the coordination ability of g-C$_3$N$_4$ to a wider variety of metals and their chemical interactions are unexploited; (iii) beyond ORR, the potential application of M–C$_3$N$_4$ for more energy related reactions is limited.

Here, using g-C$_3$N$_4$ as a platform, we investigated a series of M–C$_3$N$_4$ organometallic electrocatalysts as a new class of M–N/C materials for the aforementioned key oxygen electrode reactions. As a preliminary trial, we theoretically predicted and experimentally measured the Co–C$_3$N$_4$ complex, with a single coordinated Co atom, as an efficient electrocatalyst for the ORR and OER in alkaline media. A combination of electrochemical studies and density function theory (DFT) computation confirmed that the high activity originates from the precise Co–N$_2$ coordination moiety in the g-C$_3$N$_4$ matrix. DFT computation indicates that the catalytic ability of this new class of materials is a result of the appropriate d-band position of the catalyst.

First, we selected Co–C$_3$N$_4$ as a representative model of M–C$_3$N$_4$ since many Co–N/C materials have shown effective function toward both the ORR and OER.[7] To identify the most stable site of Co in the g-C$_3$N$_4$ matrix, geometry optimization was conducted with four possible Co locations (Figure S1a). These

initial configurations resulted in distinctively different positions of Co, in which the most stable one is where the Co atom is embedded within a void in g-C_3N_4, as suggested by its lowest relative energy. Within this structure, Co is connected to two adjacent pyridinic-N atoms from two separate triazine units, forming a CoN_3C_2 ring (Figure S1b). The charge transferred from Co to g-C_3N_4 is as high as 0.84 e⁻ based on Bader charge analysis.[8]

As shown in Figure 1a, b and Figure S2, the performances of structurally identified Co−C_3N_4 complexes as a bifunctional
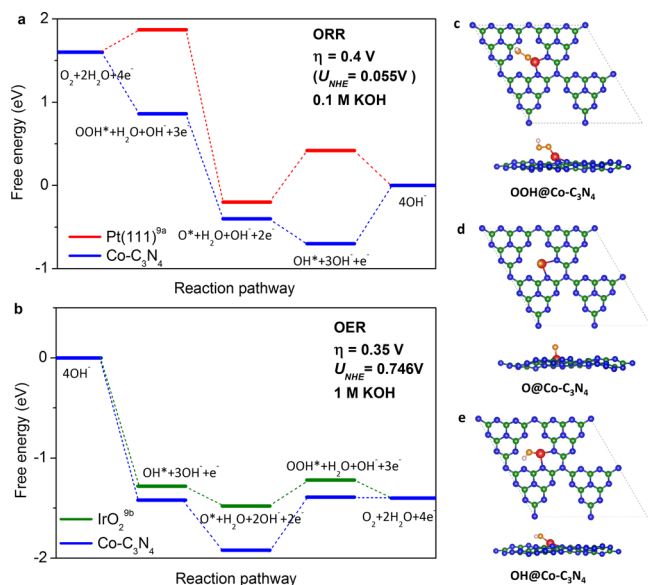

Figure 1. Free energy diagram of (a) ORR on Co−C_3N_4 and Pt (111) surfaces; and (b) OER on Co−C_3N_4 and IrO_2 surfaces. (c−e) Top and side views of atomic configurations for ORR/OER intermediate states. Green, blue, red, gold, and white represent C, N, Co, O, and H atoms, respectively.

oxygen electrode were evaluated theoretically by computing their free energy diagram for the ORR and OER under certain overpotentials (η). The choice of η was based on reported polarization curves for each reaction to simulate real conditions. For the ORR, under $\eta = 0.4$ V, all reaction steps on the Co−C_3N_4 surfaces are thermodynamically downhill except for the last one (OH* desorption), which is 0.67 eV uphill. Therefore, this step is considered to be the rate-determining-step (rds) of the overall ORR. This value is very close to that observed for benchmarked Pt(111) surfaces under the same conditions, where a 0.65 eV energy difference exists for the rds of OH* formation.[9a] In regards to the OER, under $\eta = 0.35$ V, every reaction step is downhill on Co-C_3N_4 surfaces, except for the OOH* formation step (rds), which is uphill for 0.53 eV. Also, the benchmarked IrO_2 surface follows the same mechanism with a 0.26 eV energy difference toward the rds,[9b] smaller than that of Co−C_3N_4. As shown in Figure 1c−e, the Co connected to two N atoms acts as the active center for intermediate adsorption and charge transfer in both the ORR and OER.

Proof-of-concept studies were carried out using a facile synthetic approach to prepare the Co−C_3N_4 complexes. Multiwalled carbon nanotubes (CNT) were applied as a support to enhance the electrode conductivity and to expose the electrocatalytically active sites of Co−C_3N_4. The as-prepared catalyst contained a large amount of cobalt oxide (CoO_x) nanoparticles on the CNT surface (Figure S3a). This obstructs

the identification of the real active sites in Co−C_3N_4. After acid leaching twice, most of the free-standing CoO_x was dissolved while the metal-N components remained (Figure S3b).[10] Correspondingly, the atomic concentration of Co decreased from ~2.2% to ~0.2% (Figure S3c). The final product, Co−C_3N_4/CNT, maintained the morphology of the CNT with a thin enveloping layer of g-C_3N_4 (Figure 2a). Based on the bright field
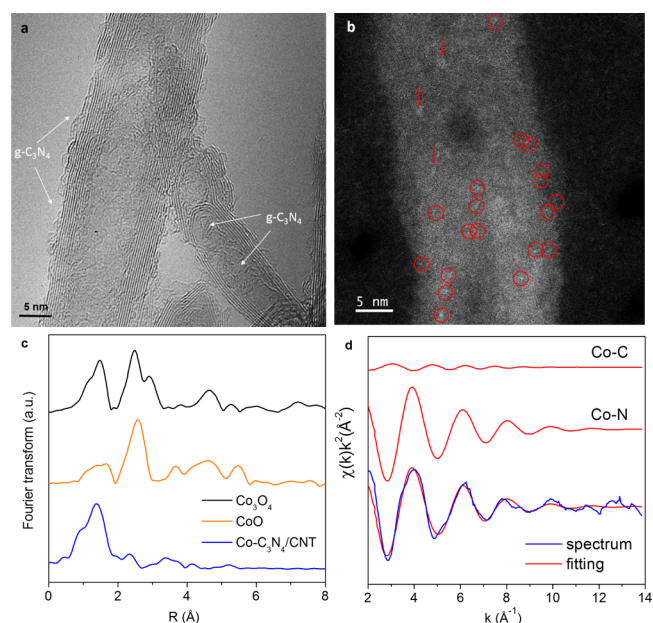

Figure 2. (a) High-resolution TEM and (b) HAADF-STEM images of Co−C_3N_4/CNT. Circles and arrows in panel b indicate single Co atoms and Co clusters, respectively. (c) Co K-edge Fourier transformed r-space EXAFS spectra of Co−C_3N_4/CNT and cobalt oxides reference samples. (d) Co K-edge k-space experimental EXAFS spectrum and fitting curves of Co−C_3N_4/CNT.

high resolution transmission electron microscopy (TEM) image, no obvious nanoparticles were found in Co−C_3N_4/CNT, indicating that most of the metal remained in the form of single atoms and clusters. The high-angle annular dark-field scanning TEM (HAADF-STEM, Figure 2b) image clearly shows the bright dots on the CNT surface that are attributed to the atomic Co components in the g-C_3N_4 matrix (note that the metal residue in the CNT was removed in advance).

Near edge X-ray absorption fine structure (NEXAFS) and extended X-ray absorption fine structure (EXAFS) spectra give accurate structural information about the Co−C_3N_4 complexes. As shown in N K-edge NEXAFS spectra (Figure S4a), Co−C_3N_4/CNT possesses the same features as g-C_3N_4.[4a] At the same time, the Co L-edge NEXAFS spectrum demonstrates two L_3-edge peaks at 778.9 and 780.2 eV (Figure S4b), which are the contribution of Co incorporating into the g-C_3N_4 matrix and bonding with N atoms (the one at 779.9 eV is from the metallic Co clusters).[10b] As shown in the Fourier transforms of Co K-edge EXAFS (Figure 2c), the peak at 1.40 Å, corresponding to Co−N scattering paths, and the peak at 2.32 Å, corresponding to Co−C scattering paths, confirm the coordination of Co and g-C_3N_4 resulting in a relative long-range order structure. Comparing this with the spectra of cobalt oxide references, no Co−O and Co−Co scattering paths are detected in Co−C_3N_4, indicating the presence of the desired Co−N local structure in the matrix. The X-ray absorption near edge structure (XANES) results (Figure S5) show that the valence of Co in the Co−C_3N_4/

CNT sample is close to that of CoO with Co(II) states. As shown in the k-space EXAFS and fitting curves (Figure 2d), the dominant contribution to the total EXAFS signal is given by the Co−N first shell while the Co−C signal is relatively weak. Based on the fitting parameters provided in Table S1, the calculated coordination number of Co is two, meaning one Co is bonded with two N atoms forming a Co−N_2 moiety. This result is also consistent with theoretical evidence, in which there are significant electron density distribution between Co and two N atoms from triazine units in the g-C_3N_4 matrix (shown later in Figure S9).

The electrocatalytic activity of the synthesized Co−C_3N_4/CNT catalyst toward ORR and OER were tested and compared to precious metal benchmarks to validate theoretical predictions. For the ORR (Figure 3a), Co−C_3N_4/CNT shows an onset
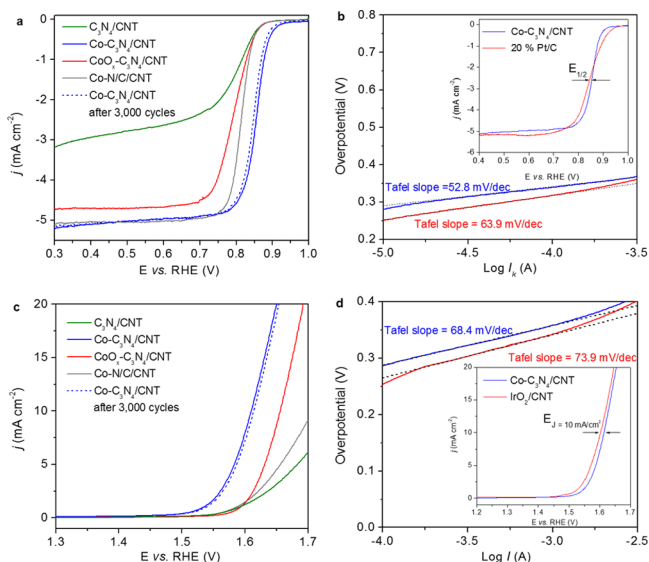

Figure 3. (a) ORR polarization curves of different Co-based catalysts in O_2-satuated KOH. The dashed curve represents Co−C_3N_4/CNT performance after a 3000 cycle (1.0 to 0.5 V) stability test. (b) Tafel plots calculated from polarization curves (inset) of Co−C_3N_4/CNT and Pt/C. (c) OER polarization curves of different Co-based catalysts in N_2-satuated KOH. The dashed curve represents Co−C_3N_4/CNT performance after a 3000 cycle (1.3 to 1.7 V) stability test. (d) Tafel plots calculated from polarization curves (inset) of Co−C_3N_4/CNT and IrO_2/CNT.

potential of ∼0.9 V (vs RHE, reversible hydrogen electrode) and a diffusion limited current density of ∼5 mA cm^{-2} in O_2-satuated 0.1 M KOH solution. The wide current plateau starting from 0.8 to 0.3 V indicates an efficient 4e$^-$ dominated ORR pathway, which has been further confirmed by the rotating ring-disk electrode test (Figure S6). For the OER (Figure 3c), Co−C_3N_4/CNT shows an onset potential of ∼1.5 V and a potential of 1.61 V to deliver an anodic current density of 10 mA/cm^2 in N_2-satuated 1 M KOH solution. These parameters indicate that Co−C_3N_4/CNT is among one of the best bifunctional ORR/OER electrocatalysts, especially for M−N/C materials.[11] Moreover, the performance of Co−C_3N_4/CNT is very comparable with precious metal benchmarks for respective ORR and OER processes judged on both overpotentials and Tafel slope values (Figure 3b, d). This gives clear validation of the activity predictions based on free energy pathway diagrams (Figure 1a, b).

Three kinds of Co-based control samples were rationally prepared and measured to identify the active sites of Co−C_3N_4/CNT as predicted by DFT computation. First, an acid leached sample of Co−C_3N_4/CNT, composed of mainly coordinated Co species, showed enhanced ORR and OER activities compared with unleached samples of CoO$_x$−C_3N_4/CNT, composed of mainly uncoordinated cobalt oxides (Figure 3a, c, Figure S7). Second, when the Co−N_2 moiety was intentionally decomposed by high temperature annealing in N_2 gas (the g-C_3N_4 framework collapses at 900 °C, converting Co−C_3N_4 to the Co−N/C complex), the product (Co−N/C/CNT) showed decreased activity in comparison to pristine Co−C_3N_4/CNT (Figure 3a, c). Third, both g-C_3N_4 coated CNT (without metal centers; C_3N_4/CNT) and Co grown on CNT (without g-C_3N_4 coordination; Co/CNT) presented lower activities than that of Co−C_3N_4/CNT (Figure 3a, c, Figure S8). Therefore, it is unambiguous that the coordinated Co species possess higher activity than uncoordinated cobalt oxide and serve as the main active site in the Co−C_3N_4/CNT electrocatalyst, similar to Co−N_x and Fe−N_x sites in M−N/C materials.[3] This coordination also grants good stability to the reversible bifunctional catalysis of Co−C_3N_4/CNT, evidenced by the miniscule performance attenuation shown in the ORR/OER polarization curves after 3000 cycles under respective test conditions (Figure 3a, c).

We then extended the study to include more 3d transition metal centered M−C_3N_4 (M = Cr, Mn, Fe, Co, Ni, Cu, Zn) composites. First, we calculated the binding energies of different metals with the g-C_3N_4 ligand to quantitatively describe their structural stabilities. As shown in Figure 4a, Fe, Ni, and Co show
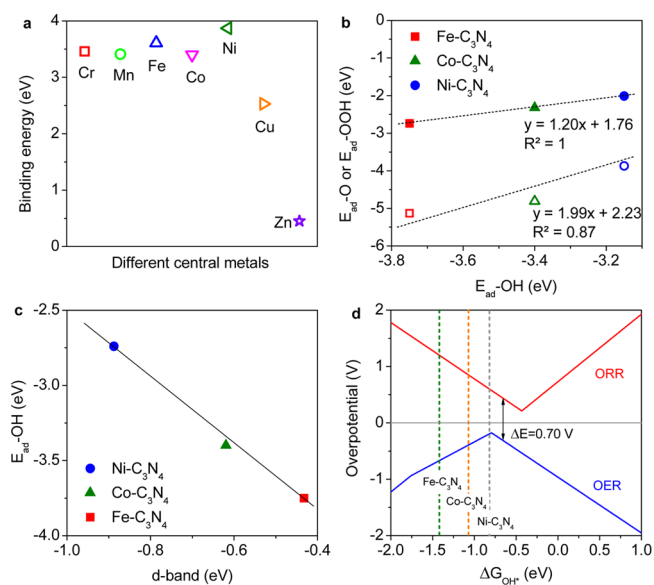

Figure 4. (a) Binding energy of various 3d transition metals in a g-C_3N_4 framework. (b) Scaling relationship of E_{ad}-OH* vs E_{ad}-OOH* (filled symbols) or E_{ad}-OH* vs E_{ad}-O* (open symbols) on M−C_3N_4 models. (c) Dependence of E_{ad}-OH* with the d-band positon on M−C_3N_4 models. (d) Dual volcano plot for ORR and OER on M−C_3N_4 models.

the strongest binding energies. Their stabilities could also be qualitatively confirmed from the electron density differences at a certain cutoff value. As shown in Figure S9, there is additional electron distribution between metal and connecting N atoms, similar to the electron distribution density around Fe on the widely studied Fe−N/C materials. Accordingly, the ORR and OER free energy diagram of Fe−, Co−, and Ni−C_3N_4 models

were then calculated and compared in Figure S10. For the ORR ($\eta = 0.4$ V), both Fe$-$C$_3$N$_4$ and Ni$-$C$_3$N$_4$ followed the same trend with that of Co$-$C$_3$N$_4$; i.e., the OH* desorption step is the rds, with all other steps being downhill. In regards to the rds, Ni$-$C$_3$N$_4$ possesses the smallest free energy difference while Fe$-$C$_3$N$_4$ possesses the largest one. For the OER, the rds for Ni$-$C$_3$N$_4$ is the O* formation step which is 0.18 eV uphill. This is different from the Co$-$C$_3$N$_4$ and Fe$-$C$_3$N$_4$ models, where, on both structures, the OOH* formation step is the rds with energy differences of 0.53 and 0.43 eV, respectively.

During the construction of free energy diagrams for these three M$-$C$_3$N$_4$ structures, a linear scaling relationship of adsorption energies (E_{ad}) between O* and OH* or between O* and OOH* was observed (Figure 4b). This trend for adsorption strength could be attributed to the electronic structure of the g-C$_3$N$_4$ coordinated with metal ligands. For example, the values of E_{ad}-OH* on all three models could be linearly related to the position of the first peak on the central metal's d-band relative to its Fermi level (Figure 4c, Figure S11). Qualitatively, a higher d-band position (e.g., Fe$-$C$_3$N$_4$ model) leads to a stronger OH* adsorption (larger absolute value of E_{ad}), while a lower d-band position (e.g., Ni$-$C$_3$N$_4$) leads to a weaker OH* adsorption (smaller absolute value of E_{ad}). Based on the above relationship, a dual volcano plot was constructed to comprehensively describe and predict the bifunctional activity toward reversible ORR/OER processes on M$-$C$_3$N$_4$ materials. The onset potential and OH* adsorption free energy (ΔG_{OH*}) for ORR/OER were employed as the activity indicators from experimental and theoretical standpoints, respectively. As shown in Figure 4d, when ΔG_{OH*} is smaller than -0.80 eV, both the ORR and OER are in the left branch of the volcano plot, indicating that the performance of both reactions is better with a weaker OH* adsorption. In contrast, when ΔG_{OH*} is greater than -0.43 eV, both the ORR and OER are in the right branch of the volcano plot, indicating better performance with stronger OH* adsorption. In the middle zone (between -0.43 and -0.80 eV), a decrease in overpotential for ORR leads to an increase in that for OER and *vice versa*. This suggests that a performance ceiling exists for M$-$C$_3$N$_4$ materials serving as bifunctional oxygen electrodes. Also, it is worth mentioning that, for a material with appropriate OH* adsorption strength within this zone, it is neither the best ORR nor OER catalyst, but shows the best bifunctional performance for reversible ORR/OER.

In summary, we evaluate M$-$C$_3$N$_4$ as a new class of nonprecious metal electrocatalysts for oxygen electrode reactions. As an example, Co$-$C$_3$N$_4$/CNT possesses comparable activities with precious metal benchmarks for the ORR and OER in alkaline media. Physicochemical and electrochemical characterization combined with DFT computation identified the active sites to be the Co$-$N$_2$ coordination moiety in the g-C$_3$N$_4$ matrix. It is demonstrated that g-C$_3$N$_4$ as a platform can coordinate a variety of metals to replace the traditional nitrogen doped carbons. We further revealed the activity origin and established a design principle for different M$-$C$_3$N$_4$ complexes.

■ ASSOCIATED CONTENT

Ⓢ Supporting Information

The Supporting Information is available free of charge on the ACS Publications website at DOI: 10.1021/jacs.6b13100.

> More materials characterization, electrochemical measurements, computational models and methods (PDF)

■ AUTHOR INFORMATION

Corresponding Author
*s.qiao@adelaide.edu.au

ORCID Ⓞ
Yan Jiao: 0000-0003-1329-4290
Ying Chen: 0000-0002-7322-2224
Shi-Zhang Qiao: 0000-0002-4568-8422

Author Contributions
‖Y.Z. and Y.J. contributed equally.

Notes
The authors declare no competing financial interest.

■ REFERENCES

(1) (a) Jiao, Y.; Zheng, Y.; Jaroniec, M.; Qiao, S. Z. *Chem. Soc. Rev.* **2015**, *44*, 2060. (b) Stephens, I. E. L.; Bondarenko, A. S.; Gronbjerg, U.; Rossmeisl, J.; Chorkendorff, I. *Energy Environ. Sci.* **2012**, *5*, 6744.

(2) (a) Chen, Z.; Higgins, D.; Yu, A.; Zhang, L.; Zhang, J. *Energy Environ. Sci.* **2011**, *4*, 3167. (b) Artero, V.; Chavarot-Kerlidou, M.; Fontecave, M. *Angew. Chem., Int. Ed.* **2011**, *50*, 7238. (c) Han, L.; Dong, S.; Wang, E. *Adv. Mater.* **2016**, *28*, 9266.

(3) (a) Jiang, W.-J.; Gu, L.; Li, L.; Zhang, Y.; Zhang, X.; Zhang, L.-J.; Wang, J.-Q.; Hu, J.-S.; Wei, Z.; Wan, L.-J. *J. Am. Chem. Soc.* **2016**, *138*, 3570. (b) Zitolo, A.; Goellner, V.; Armel, V.; Sougrati, M.-T.; Mineva, T.; Stievano, L.; Fonda, E.; Jaouen, F. *Nat. Mater.* **2015**, *14*, 937.

(4) (a) Zheng, Y.; Jiao, Y.; Zhu, Y.; Li, L. H.; Han, Y.; Chen, Y.; Du, A.; Jaroniec, M.; Qiao, S. Z. *Nat. Commun.* **2014**, *5*, 3783. (b) Zheng, Y.; Liu, J.; Liang, J.; Jaroniec, M.; Qiao, S. Z. *Energy Environ. Sci.* **2012**, *5*, 6717.

(5) (a) Wang, X.; Chen, X.; Thomas, A.; Fu, X.; Antonietti, M. *Adv. Mater.* **2009**, *21*, 1609. (b) Zou, X.; Su, J.; Silva, R.; Goswami, A.; Sathe, B. R.; Asefa, T. *Chem. Commun.* **2013**, *49*, 7522. (c) Zou, X.; Huang, X.; Goswami, A.; Silva, R.; Sathe, B. R.; Mikmeková, E.; Asefa, T. *Angew. Chem., Int. Ed.* **2014**, *53*, 4372.

(6) (a) Jin, J.; Fu, X.; Liu, Q.; Zhang, J. *J. Mater. Chem. A* **2013**, *1*, 10538. (b) Liu, Q.; Zhang, J. *Langmuir* **2013**, *29*, 3821.

(7) (a) Liang, Y.; Li, Y.; Wang, H.; Zhou, J.; Wang, J.; Regier, T.; Dai, H. *Nat. Mater.* **2011**, *10*, 780. (b) Wang, Z.; Xiao, S.; Zhu, Z.; Long, X.; Zheng, X.; Lu, X.; Yang, S. *ACS Appl. Mater. Interfaces* **2015**, *7*, 4048. (c) Gadipelli, S.; Zhao, T.; Shevlin, S. A.; Guo, Z. *Energy Environ. Sci.* **2016**, *9*, 1661.

(8) Henkelman, G.; Arnaldsson, A.; Jónsson, H. *Comput. Mater. Sci.* **2006**, *36*, 354.

(9) (a) Liu, S.; White, M. G.; Liu, P. *J. Phys. Chem. C* **2016**, *120*, 15288. (b) Sun, W.; Song, Y.; Gong, X.-Q.; Cao, L.; Yang, J. *Chem. Sci.* **2015**, *6*, 4993.

(10) (a) Kramm, U. I.; Herrmann-Geppert, I.; Behrends, J.; Lips, K.; Fiechter, S.; Bogdanoff, P. *J. Am. Chem. Soc.* **2016**, *138*, 635. (b) Bayatsarmadi, B.; Zheng, Y.; Tang, Y.; Jaroniec, M.; Qiao, S. Z. *Small* **2016**, *12*, 3703.

(11) (a) Gupta, S.; Kellogg, W.; Xu, H.; Liu, X.; Cho, J.; Wu, G. *Chem. - Asian J.* **2016**, *11*, 10. (b) Kuang, M.; Zheng, G. *Small* **2016**, *12*, 5656.